Ozone detection in the ppt-level with rGO-ZnO based sensor

Bruno Sanches de Lima, Amanda Akemy Komorizono, Weverton Alison dos Santos Silva, Jerome Brunet, Amadou Ndiaye, Maria Bernardini, Valmor Roberto Mastelaro

Ozone detection in the ppt-level with rGO-ZnO based sensor

B. S. de Lima*[1, 2], A. A. Komorizono[1], W. A. S. Silva[1], A. L. Ndiaye[2], J. Brunet[2], M. I. B. Bernardi[1], V. R. Mastelaro[1]

[1]Sao Carlos Institute of Physics, University of Sao Paulo, 565-905 São Carlos, SP, Brazil

[2]Université Clermont Auvergne, CNRS, SIGMA Clermont, Institut Pascal, F-63000 Clermon-Ferrand, France

ABSTRACT

Although several studies have explored the rGO-ZnO nanocomposites gas sensing properties towards many gases, only a few are devoted to ozone detection. This paper explores a novel synthesis procedure of rGO-ZnO nanocomposites based upon a two-step physical process. Namely, a reduction process of GO carried out using UV laser radiation followed by a deposition of ZnO nanoparticles on the rGO surface by RF-magnetron Sputtering. Our results demonstrate that the deposition of ZnO on the surface of the rGO film produces a stable and conductive material with a larger surface area. Consequently, this material is able to operate at high temperatures and exhibited a limit of detection (LOD) in the range of 100 ppt, while pure ZnO exhibited LOD in the vicinity of 1 ppb.

Keywords: rGO, nanocomposite, ZnO, laser processing, gas sensor, ozone

**Corresponding Author:* delima.bs@gmail.com, delima.bs@usp.br

1. INTRODUCTION

Since the isolation of monolayer graphene in 2004, its remarkable physical properties related to the low dimensionality and Dirac fermions in the electronic structure [1, 2] have made graphene-related materials a major research topic in materials sciences [3]. Pristine graphene still faces considerable challenges for real applications due to the difficulties for large scale production of devices as processing usually requires high temperature, high vacuum [4, 5], and transfer steps that can significantly deteriorate its physical properties [6].

Among all the nanocarbonaceous materials, two graphene-related have been extensively studied, graphene oxide (GO) and reduced graphene oxide (rGO). These materials are commonly produced by chemical routes that use ordinary oxidizing and reducing agents [7, 8]. The GO can be depicted as a two-dimensional (2D) array of carbon atoms forming the typical hexagonal graphene structure with oxygenated groups, such as hydroxyls, epoxies, or carboxyls, that bonded to the main hexagonal C structure. In contrast, rGO has a very similar structure but has a significantly lower amount of these oxygenated groups. It is important to mention that these oxygen-rich functional groups bond covalently to the π electrons of the C-sp^2 hybrid orbitals that are the entities responsible for electrical conduction in pristine graphene. Hence, GO has a higher electrical resistance as compared to rGO and pristine graphene. Thus, removing these oxygenated groups of the GO structure restores some of the pristine graphene properties in rGO [8]. The modulation of the density of these oxygenated groups has opened the way to many potential applications for rGO, such as supercapacitors for energy storage [9, 10], chemical sensors [11, 12], biosensors [13] as well as photocatalyst [14]. Although rGO exhibits high potentialities for various applications, fundamental physical properties such as electronic mobility or thermal conductivity are significantly lower than those intrinsic to pristine graphene due to the remaining oxygenated groups in the structure and high density of crystalline defects [15]. Such drawbacks can affect the performance of devices.

To overcome these limitations, rGO can be combined with different materials to modify its physical properties in a synergetic manner regarding its physical properties, such as nanostructured semiconductor metal oxides. For instance, a nanocomposite fabricated by SnO_2 nanoparticles' addition to rGO exhibited higher sensitivity towards humidity [16]. SnO_2-rGO nanocomposites were also explored as sensing elements for NO_2 detection operating at room temperature. It was

established that the addition of SnO_2 could increase the NO_2 response at 50°C by a factor of 3 [17]. Andre *et al.* [18] have reported that nanocomposites based on In_2O_3 nanofibers and rGO are 10 times more sensitive than pure rGO or pure In_2O_3 nanofibers regarding the detection of NH_3. rGO-In_2O_3 nanocomposites have also been successfully explored as NO_2 sensing materials [19-21]. The morphology and elements' proportion of these nanocomposites play an important role in its outcome properties. The work of Woong Na *et al.* [20] reported that rGO nanosheets decorated with In_2O_3 nanoparticles exhibit a response of 30 at 120°C when exposed to 500 ppb NO_2, while Liu *et al*. [21] produced flower-like nanostructures that could detect 1000 ppb at 70°C with response higher than 1000.

For gas detection applications, ZnO is a relevant metallic oxide that has been associated with rGO to develop superior sensing nanocomposites [22, 23]. For instance, 3D structures of rGO decorated with ZnO nanoparticles exhibit a sensitivity of 85% for CO detection with high selectivity [24]. Anasthasiya *et al.* [25] demonstrated that rGO decorated with ZnO nanowires has a much higher and faster response towards NH_3 detection at room temperature than pure ZnO nanowires. rGO nanosheets decorated with Ni-doped ZnO nanowires were also tested for hydrogen detection, exhibiting approximately 30% of response operating at 150°C [26]. More recently, rGO decorated with Cu-doped ZnO nanocomposites were used to detect H_2S at room temperature in concentrations lower than 250 ppm [27]. Some ternary nanocomposites have also been investigated. In this case, metal nanoparticles are added as a source of free carriers that may act as a source of free charge (Schottky junction) for the metal oxide semiconductor, consequently enhancing the number of available charges gaseous species adsorption. This approach produced highly sensitive layers of Au-rGO-ZnO for triethylamine [28] and hydrogen [29] operating at 50°C and room temperature with UV radiation. Another ternary nanocomposite based upon Pt-rGO-ZnO was tested for hydrogen detection by Drmosh and collaborators [30]. This nanocomposite was faster and benefited from higher sensitivity than pure ZnO when operating at similar temperatures.

While the sensing potentialities of rGO-based materials have been well-established for many reducing gases such as H_2, NH_3, and oxidizing gases such as NO_2, few results are available towards ozone (O_3). The interaction of O_3 on rGO-ZnO nanocomposites has been only explored by Jayachandiran *et al.* [31]. Their results show that the rGO-ZnO nanocomposites exhibit room temperature response of 99% for 0.7 ppm of O_3.

Ozone (O_3) is an allotropic form of oxygen with great UV radiation absorption and oxidation capacity. Due to these reasons, ozone has great importance for life maintenance as the main UV shield at the so-called ozone layer in the stratosphere. Due to its strong oxidizing capacity, it is the primary disinfectant agent used worldwide [32]. On the ground level, ozone is an aggressive, toxic gas that can cause severe lung damage to a person exposed to O_3 concentrations as low as 150 ppb. The ground-level ozone forms after nitrogen oxides (NO_x) and Volatile Organic Compounds (VOCs) in the presence of UV radiation and is considered as the second most present pollutant in urban areas [33]. For this reason, the World Health Organization (WHO) Air Quality Guidelines of 2005 has established the limit for O_3 exposure as 100 ppb during an 8-hour period. The most used ozone monitoring technologies are based on UV photometric analyses, which typically have a limit of detection of 100 to 500 ppt. However, these devices are non-portable, expensive, and required air-conditioned stations. O_3 monitoring technologies based on semiconductor metal oxides or electrochemical principles commercially available typically exhibit a lower detection limit in the range of 10 to 50 ppb. As a consequence, semiconductor metal oxides based O_3 sensing technologies are still close to the safe levels determined by the WHO. New O_3 monitoring technologies should be inexpensive, easy to operate, be compatible with IoT devices, and have a lower limit of detections to yield reliable readings at the levels considered safe by the WHO in real-time.

Most of the previous publications mentioned here report nanocomposite synthesis procedures based on hydrothermal approaches. In these studies, the rGO and a metal oxide liquid precursor are held together inside teflon/stainless steel chambers. The chamber is then heated up to temperatures higher than 100°C to form metal oxide nanoparticles and keep the rGO sheets stable [16, 17, 19-21, 24, 26, 27]. Physical methods for nanocomposites synthesis are more commonly used when metal nanoparticles are desired to decorate the rGO layers [28, 29].

In the present study, rGO-ZnO nanocomposites are synthesized using a two-step fabrication procedure consisting of reducing GO films by UV-laser irradiation and decorating them with ZnO nanoparticles (NP) by RF-magnetron sputtering deposition technique. This fabrication procedure allowed us to control the size and the morphology of ZnO nanoparticles finely. The ZnO nanoparticles act as a temperature protective layer to the rGO nano-sheets, which allows the nanocomposite to be operated at high temperatures. Regarding its ozone sensing performance, our

results suggest that the nanocomposite has a limit of detection ten times greater than a pure ZnO film and reaching significant responses at the ppt level.

2. EXPERIMENTAL

2.1. rGO-ZnO nanocomposites elaboration

Figure 1(a) presents a schematic drawing of the elaboration protocol of the rGO-ZnO nanocomposites. At first, an aqueous solution of graphene oxide (4 mg/mL purchased from Sigma Aldrich) was diluted to 1 mg/mL. Then, this solution was drop-casted on silicon substrates and let into the atmosphere to dry. Each drop cast cycle used a solution volume of 25 μL of the diluted GO solution. The drop-casting process was carried out carefully to keep the material covering an area of ~ 5 mm of diameter on the interdigitated electrodes for the sensing device fabrication. The reduction process was carried out using a Spectron SL400 Q-switch laser system in which the pulse duration and wavelength were set to 6 ns and 266 nm, respectively. The silicon substrates with the deposited GO films were placed on an XY table that scanned the films with the unfocused beam covering an area of 5 mm and energy fluence set up to 50 mJ/cm^2. The scanning rate was set to 1 mm/s to avoid material overheating, and the scanning procedure was repeated five times to achieve better chemical homogeneity. After the reduction process, the films were introduced into an RF-magneton sputtering chamber for metallic zinc deposition. The chamber was kept under high-vacuum ($5x10^{-6}$ mbar) for one hour, and the working pressure was set to $2.5x10^{-2}$ mbar and RF power at 60 W. The amount of Zn deposited was controlled by the deposition time. In our experimental conditions, the deposition rate was estimated at 40 nm/min (2.5 min to 100 nm film). The substrates were then heat-treated at 500°C under air for one hour to complete the Zn oxidation and form the junction with rGO. The heating rate used in this oxidation process was 2.5ºC/min.

2.2. Material characterizations

X-ray diffraction data were collected in a Rigaku Ultima IV diffractometer equipped with a Cu target, Cu-Kα radiation (λ = 1.5418 Å), and Ni filter. The data were obtained between 2θ = 20 and 80, and the analysis was carried out using GSAS-II [34], PowderCell [35], and Vesta

Crystallography [36]. Micro Raman spectroscopy experiments were carried out in a Witec microscope equipped with a Nikon objective and the samples were excited by an ion Ar laser (wavelength of 514 nm). The Raman spectra data were recorded with a Peltier cooled CCD system. Scanning Electron Microscopy images were obtained in a Field-Emission Supra 35-VP Carl Zeiss operated at 15 kV. X-ray photoelectron spectroscopy (XPS) measurements were carried out in a Scienta Omicron ESCA spectrometer with monochromatic X-ray source Al-Kα. The observed peaks were fitted using a Voigt function after subtracting a Shirley background. In the fitting procedure, the spectra were corrected considering the C-sp^2 component with energy at 284.5 eV.

2.3. *Ozone sensing properties evaluation*

Figure 1(b) represents the experimental setup used to measure the gas sensing properties under pollutant gases. The sensing properties were determined by the continuous monitoring of the electrical resistance variations of films prepared over the Pt interdigitated electrodes during exposures to well-controlled ozone concentrations between 10 ppb and 1 ppm. The sensing substrates were placed on a PID controlled hot plate, and a thermocouple used for temperature control was kept close to the sample. The electrical resistance was calculated by the ratio of the electrical current measured between the two electrodes by a Keithley 6514 electrometer and excitation voltage of 5 V d.c. applied by a Tektronix PWS4205 voltage source. Before the measurements, the films were maintained under dry airflow kept at 100 sccm for 4 hours for temperature and resistance stabilizations. The Mass Flow Controllers, electrometer, voltage source, and temperature controller were connected to a computer dedicated to experimental controlling and data acquisition. During the exposure step, O_3 was generated by exposing the dry airflow under UV radiation (lamp UVP, model P/N 90-0004-01), and the real concentrations were determined by an ATI (model F12) commercial electrochemical based gas detector. The sensor response is defined as the ratio between the resistance under O_3 and under air (R_{O3}/R_{air}). The response/recovery times are defined as the time necessary to reach 90% of ΔR induced by pollutant concentrations during gas exposure and consecutive recovery under dry air.

3. RESULTS AND DISCUSSION

3.1. Surface and structure characterizations

Figure 2 presents XRD data and Raman spectra of GO, rGO, Zn, ZnO, and rGO-ZnO nanocomposites. Figure 2(a) shows that the most significant difference between GO and rGO diffraction patterns is the intensity of GO's characteristic peak related to the oxidized planes of graphite. The intensity difference is related to ablation during the laser reduction process, leading to a lower amount of diffracting planes. In the case of GO, this peak occurs at $2\theta = 9.5°$ while in rGO, it occurs at $2\theta = 9.7°$. Using Bragg's law, one can estimate the distance between the (001) planes for GO and rGO in 9.3 and 9.1 Å. The lower plane distance observed in rGO is related to fewer oxygenated functional groups in these planes [8]. The same figure presents the diffraction pattern of metallic zinc observed right after the RF-magnetron sputtering deposition, and the typical pattern obtained after these films were heat-treated at 500°C for one hour. It is important to mention that both metallic Zn and ZnO crystallize in hexagonal symmetries with different space groups, $P6_3/mmc$ (194) and $P6_3mc$ (186), respectively. After the oxidation process, it is observed that there is no remaining diffraction peak in the oxidized sample, which suggests that the oxidation condition successfully converted all the metal to a ZnO film. The figure also includes the diffraction pattern of a sample prepared after reducing 25 μL GO and 1 μm thick film of ZnO on the rGO surface. Since crystalline compounds have a higher capacity of X-ray scattering, it is expected that these samples will present a similar X-ray diffraction pattern similar to the one observed for only ZnO, as the peak for rGO should be close to the background level.

To better understand the structural features of these nanocomposites, Raman spectroscopy measurements were also performed. The spectra of GO, rGO, and rGO-ZnO are shown in figure 2(b). This technique has been widely used to characterize graphene-related materials because it is non-destructive and sensitive to distinguish carbonaceous materials [37]. For the GO and rGO data, the most important vibrational bands are the D (~ 1350 cm^{-1}), related to the presence of crystalline defects. The G_{app} (~ 1610 cm^{-1}) stands for G apparent and refers to the G and D' bands' convolution. The G band is present in graphene, graphite, carbon nanotubes, and fullerenes, as it is related to the vibration of C-sp^2. Another important band is 2D (~2680 cm^{-1}), the G band second-order vibration mode related to the formation of aromatic rings. An increase in this band intensity

is often connected to the formation of aromatic rings in the sample. For instance, this band in pristine graphene is twice as intense as the G band due to resonant effects [37]. Data reported in Figure 2(b) shows that the 266 nm laser reduction process presents a significant increase in the resonant electrons due to the aromatic rings in rGO, which will grant this compound higher electrical conductivity. The deposition of ZnO on the surface of rGO can be verified in the orange and green curves in Figure 2(b), as the intensity of the vibration modes related to ZnO increase when the amount of ZnO is increased. It is important to mention that major features in the ZnO Raman spectra are the bands at 330, 438, 530, 580, 1110, and 1157 cm^{-1}. The one observed at 330 cm^{-1} results from a multi-phonon combination of the E_2 phonon modes related to the vibration of the Zn and O sub-lattices, namely, E_2^{low} at 99 cm^{-1} (not shown) and E_2^{high} at 438 cm^{-1}. The peaks at 530, 1110, and 1157 are second-order modes, while the peak at 580 cm^{-1} can be attributed to a longitudinal optical mode A1(LO). Other peaks are expected in this region, but the proximity does not allow one to separate all the components [38].

Figure 3 reports the surface characterization of GO, rGO, pure ZnO, and rGO-ZnO nanocomposites through X-ray Photoelectron Spectroscopy (XPS). On the survey spectra depicted on the left panel, Figure 3(a), a significant decrease in the magnitude of the O 1s peak observed on rGO films compared to GO films is manifest. Such a decrease is attributed to the laser reduction process. In these samples, the amount of O in the surface decreased from 34.9 to 2.7. Furthermore, the remaining sulfur due to the chemical exfoliation process to produce GO was eliminated after the laser reduction process. For the rGO-ZnO nanocomposite, the amount of oxygen and carbon accounts for 41.0 and 45.6 %, respectively, while for the pure ZnO film, these values are 36.1 and 56.4 %. Figure 3(b) shows the high-resolution C-1s spectra for these samples. The C-1s peak was fitted with five components, namely, C-C sp^2 (284.5 eV), C-C sp^3 (~ 285 eV), C-O-C (~ 286.9 eV), C=O (~ 288 eV), COOH (~ 289 eV). The relative intensity of the oxygenated groups decreased significantly after the laser reduction process. Indeed, GO exhibit 10.3 % of C-C sp^2, 23.5 % of C-C sp^3, 50.8 % of C-O-C, 11.5 % of C=O, and 3.9 % of COOH, while the same components represent 46.5, 29.2, 12.4. 6.7 and 5.2 % for rGO, respectively. Concerning data relative to the ZnO sample, the C 1s peak can be fitted with the same components, showing the most intense peak related to the C sp^2 component. The rGO-ZnO sample exhibited the major component as the C-C sp^3 due to the sum of C sp^3 from the rGO and adventitious carbon. In Figure 3(c), the high-resolution spectra of O 1s are shown for each sample. For GO and rGO samples, the

O 1s peak comprises only one component related to oxygen atoms bonded to carbon, assuming no detectable difference between different O components bonded to C. For the pure ZnO sample, this component can be deconvoluted into three components: first contribution at 530.1 eV related to ZnO structural oxygen, second contribution at 531.1 eV that can be attributed to weakly adsorbed species at the surface, such as OH, and the third component at the higher energy of 532.4 eV that are related to C-O bonds from adventitious carbon. Furthermore, these components account for 62.0, 29.3, and 8.7 % of the oxygen on the surface, agreeing with the literature [39, 40]. The O 1s peak observed in the rGO-ZnO sample could be fitted with the same three components, but in this case, the most intense component is related to the weakly adsorbed species, which strongly suggests a higher surface area than pure ZnO films. In this sample, the first component related to ZnO structural oxygen represents 42.1 %, while weakly adsorbed species and C-O represents 44.4 and 13.5 %. It is important to mention that the valence band edge (data not shown) was estimated at 3.7 eV for pure ZnO and 2.6 for rGO-ZnO nanocomposites, suggesting that the rGO-ZnO samples may exhibit a higher density of states and narrower gap than pure ZnO [41-43].

Figure 4 presents SEM micrographs of rGO-ZnO nanocomposites. In Figure 4(a), one can observe the typical GO sheet-like microstructure, in which a smooth surface exhibit the formation of wrinkles as a result of several GO layers pilling up after the deposition process. Figures 4(b) and 4(c) show SEM images obtained with different magnifications of a GO film after its reduction by laser irradiation. In these figures, one should note that the rGO layers are much more porous than the original GO and further that the laser irradiation process induces the formation of laser-induced periodic surface structure (LIPSS) as a consequence of deoxygenation of the GO layers, as pointed out for Yung and collaborators [44]. Figures 4(d) and 4(e) present two different magnifications of a sample prepared after the deposition of a 100 nm thick ZnO film over the rGO. It is possible to observe that the original rGO structure is preserved, and it is decorated with nanoparticles with a mean diameter of 55 nm. Upon deposition of 1 μm thick film of ZnO, it is possible to observe that the deposited nanoparticles' average mean size increased to 98 nm. The morphology of a sample prepared after the deposition of 1 μm thick film of ZnO on the rGO surface is shown in Figure 4(g) and 4(h). The particle size distribution of these two samples is shown in Figures 4(f) and 4(i).

3.2. Sensing performances towards O_3 detection

Figure 5 presents the dynamic response-recovery curves obtained by monitoring the sensor's resistance upon O_3 controlled exposure at 200 and 300°C for rGO, ZnO, and rGO-ZnO. Figure 5(a) shows the resistance data obtained from a pure laser rGO sample maintained at 200°C and exposed to four cycles of 100 ppb of O_3 for three minutes. Interestingly, one can observe an increase in the electrical resistance upon ozone exposure, which strongly suggests that the laser reduced GO samples are n-type semiconductors in contrast with typical rGO obtained by chemical or thermal reducing methods. Indeed, it was already demonstrated that the semiconducting nature of rGO strongly depends on the remaining oxygenated groups bonded to the rGO hexagonal structure [45]. Similar behavior has also been observed by room temperature UV-laser irradiation of rGO films by A. Bhaumik and J. Narayan [46]. They interpret that the rGO semiconducting nature depends on the laser fluence (energy/area) used in the reduction process, and the conversion to n-type is related to structural reorganization yielded by the laser-induced conversion of carbon-sp^3 to sp^2. For the pure rGO sample, the sensor response to O_3 is very low, approximately 0.001 or 0.1%, with slow recovery kinetics due to weak reversibility of response even at 200°C. An irreversible alteration of the carbonaceous matrix can result from an interaction with ozone, leading to a cumulative increase in resistance after exposure. Indeed, it is well-known that O_3 can break C=C bonds through an ozonolysis process and be used to increase the oxidation degree of GO with a possible decomposition stage at room temperature [47], for example. Here, we argue that this reaction causes a permanent degradation of the conductive properties of rGO, leading to a decrease in the density of the adsorption sites.

Figure 5(b) shows the response-recovery curves for pure ZnO maintained at 200°C and exposed to 100 ppb of O_3 with a consecutive period and dry air. We can notice that after 3 minutes (180s) of O_3 exposure, the response was approximately equal to 3, and no plateau for the resistance was reached. By comparing both curves, ZnO's sensitivity is higher than of pure rGO, as expected from the literature, even though no saturation of the resistance was observed after 20 minutes of exposure. As illustrated in Figure 5(c), the deposition of ZnO on the surface of rGO enhances sensitivity and the kinetics of the surface reaction as compared to rGO and ZnO separately. For 70 ppb of ozone exposure during 3 minutes, the sensor response was 9, and no saturation was observed after 10 minutes of exposure. Our results suggest that the association of ZnO and rGO into a

composite is synergic for sensing applications because the sensing performance of the nanocomposite is superior to the performance obtained for each material tested separately.

In order to confirm the sensing potentialities towards O_3, the sensing behavior was explored under other concentrations at 300°C, as reported in figures 5(d), 5(e), and 5(f). It is well known that the typical operation temperature for gas sensors based on semiconductors metal oxides range between 200 and 400°C or more because the kinetics of the surface reaction usually depends on the adsorption of O_2 in the form of O^- ions. Similarly, the O_3 absorption process at this temperature range depends on O^- ions adsorption rate [48]. The following reactions describe the mechanisms of adsorption of O_2 and O_3 on semiconductor metal oxides (SMOx):

$$O_{2(g)} + 2e^-_{(surface)} \rightarrow 2O^-_{(surface)} \quad (1)$$

$$O_{3(g)} + 2e^-_{(surface)} \rightarrow O_{2(g)} + O^-_{(surface)} \quad (2)$$

As these reactions depend on the density of free electrons at the surface, the higher the operating temperature, the higher the semiconductor carrier density, and more significant changes in the electrical conductivity resulting from a more intense surface charge transfer between the semiconductor and the gas. A typical response-recovery curve of a 100 nm thick ZnO thin film is shown in Figure 5(d). At 300°C, one can observe a much higher and faster response-recovery curve by comparing these results to the one at 200°C, shown in Figure 5(b). For instance, the response time at 300°C is estimated to 85 seconds for 140 ppb exposure, whereas it exceeded 1200 s at 200°C. In Figures 5(e) and 5(f), the response-recovery curves of nanocomposites prepared by 1 and 3 drop-cast cycles of GO followed by 100 nm deposition of ZnO are shown. In other words, the proportion of rGO increases from Figure 5(d) to 5(f). Interestingly, while pure ZnO has a response of 35 to 140 ppb of O_3, the 1rGO-ZnO response is 61, and 3rGO-ZnO has a response of 71 for the same O_3 concentration level.

The sensing behavior of these nanocomposites is further analyzed in Figure 6. The dynamic response-recovery curve for ~ 100 ppb exposure of O_3 is shown in detail in Figure 6(a). It is possible to observe that not only the response of 3rGO-ZnO nanocomposite is higher, but also its response and recovery times are significantly lower than pure ZnO. These results suggest that both the adsorption and desorption kinetics are enhanced by the association of ZnO with rGO layer.

Figure 6(b) shows that the resistance change ratio is also dependent on the ozone concentration. The higher response exhibited by rGO-ZnO samples compared to ZnO layers can be justified by the larger specific surface area provided by rGO sub-layer that induces a greater number of available adsorption sites. The higher rates of adsorption and desorption strongly support that these adsorption sites are more easily accessible as well as reversible for gas adsorption in contrast with ZnO layer exhibiting a lower surface/volume ratio as noticeable from the SEM images shown in Figure 4. Thus, we attribute this enhancement in sensing performances to a higher surface area promoted by the porous surface of rGO from the UV-laser processing. Consequently, the response to other oxidizing gases like NO_2 should also be enhanced, leading to a selectivity comparable to pure ZnO.

Figure 6(d) shows the maximum resistance change rate's dependence as a concentration function in both adsorption and desorption. Hence, the change rate in resistance can also be used as a more sensitive parameter to the ozone sensing phenomenon. According to the Theory of the Power law proposed by Yamazoe and Shimanoe [48], the response of a SMOx-based sensor response towards a reactive gas is described by a power law as $R = aC^n$, in which R and C represent the response and gas concentration or partial pressure, a and n are constants. By fitting the data shown in Figure 6(c), the ZnO film's response is described by $R = 2.9\ C^{0.51}$, while the 3rGO-ZnO film is fitted with $R = 7.5C^{0.41}$. According to the International Union of Pure and Applied Chemistry (IUPAC), the definition of LOD is the analyte concentration that gives a response three times higher than the standard deviation (σ) of measurement without the analyte target. Considering the standard deviation of baseline measurements shown in Figure 5, one can find $\sigma = 0.03$, which yields LOD equals to 0.15 and 0.01 ppb for ZnO and rGO-ZnO, respectively. For comparisons purposes and more clear data visualization, we have decided to use a more conservative approach to estimate the LOD and considered the minimum detectable concentration as the concentration that would have a response equals 3 ($R_{O3}/R_{air} = 3$), represented by a horizontal line in the inset of Figure 6(c). By this approach, the estimation of LOD is 1 ppb and 0.1 ppb (100 ppt) for ZnO and rGO-ZnO, respectively. In both scenarios, the LOD of the nanocomposite is at least ten times higher than the ZnO separately. Table 1 reports the sensing performances of our nanocomposite compared to other recent developments of metallic oxides as sensing nanomaterials for efficient ozone measurement. Even though this device does not work at room temperature, the ZnO-rGO bilayer structure exhibits a significant sensitivity towards O3 compared to those

determined in the same concentration range. Many efforts remain required to make this sensing structure selective to discriminate O_3 from NO_2.

Because selectivity and stability are crucial issues for gas sensors, the interference of humidity on our nanocomposites' gas sensing properties should be investigated. It is well-known that humidity can affect SMOx-based gas sensors according to a mechanism that differs from one oxide from another. On the one hand, it has demonstrated that humidity acts as an oxidizing species on WO_3, leading to a competition for adsorption between water vapor other oxidizing gases [49]. Consequently, its presence decreases the WO_3-based sensors' response towards oxidizing pollutants. On the other hand, on SnO_2, humidity interacts as a reducing analyte, which would enhance its response for oxidizing gases [50, 51]. A recent study has determined that humidity acts as a reducing gas on ZnO at high temperatures as it decreases the response of these oxides towards CO and H_2 [52]. Other studies have also shown that ZnO responses increase towards oxidizing gases such as NO_2 [53]. Since our devices have an active surface composed of ZnO, it is expected that humidity would also act as a reducing gas, enhancing its response towards ozone. Further experimentation would be necessary to precisely assess its influence on these nanocomposites' gas sensing properties and would be the topic of a next paper.

4. CONCLUSIONS

In summary, this work reports a new synthesis procedure to prepare rGO-ZnO nanocomposites based upon physical methods. Our results demonstrated that the ns pulsed UV laser irradiation of GO films reduces the amount of oxygenated functional groups of GO from 35 to 2.8% and has the capacity to partially restore the C-sp^2 hexagonal resonating structure typical of pristine graphene. The rGO-ZnO nanocomposite fabrication was carried out by the deposition of ZnO on the surface of laser rGO by magnetron sputtering. This procedure allows one to precisely control the ZnO nanoparticles' amount, morphology, and size. Furthermore, this fabrication approach allowed the rGO-based nanocomposite to operate at higher temperatures because the ZnO layer acts as a shield to the rGO layer, preventing its direct contact with the atmosphere. Moreover, it benefits from the extended active surface area providing by rGO highly porous layer for adsorption enhancement. Our results open perspectives to further explored rGO-based nanocomposites on MEMS-based devices. Regarding the ozone sensing properties of these

nanocomposites, our results demonstrated that the deposition of ZnO nanoparticles in the surface of the laser rGO improves the response significantly and resistance change ratio when compared to pure ZnO or rGO. This improvement is related to a higher surface area and density of states of the nanocomposites allowing higher and faster O_3 adsorption. Consequently, the ZnO limit of detection could be enhanced by a factor of 10 if the ZnO nanoparticles are deposited over the rGO surface.

ACKNOWLEDGMENTS

This work is based upon Sao Paulo Research Foundation's financial support – FAPESP (grants Nº 2018/07517-2, 2019/22899-1, and 2013/07296-2). The authors are also thankful to the Brazilian National Science Financial Agencies CNPq and Capes.

LIST OF FIGURES

GRAPHICAL ABSTRACT

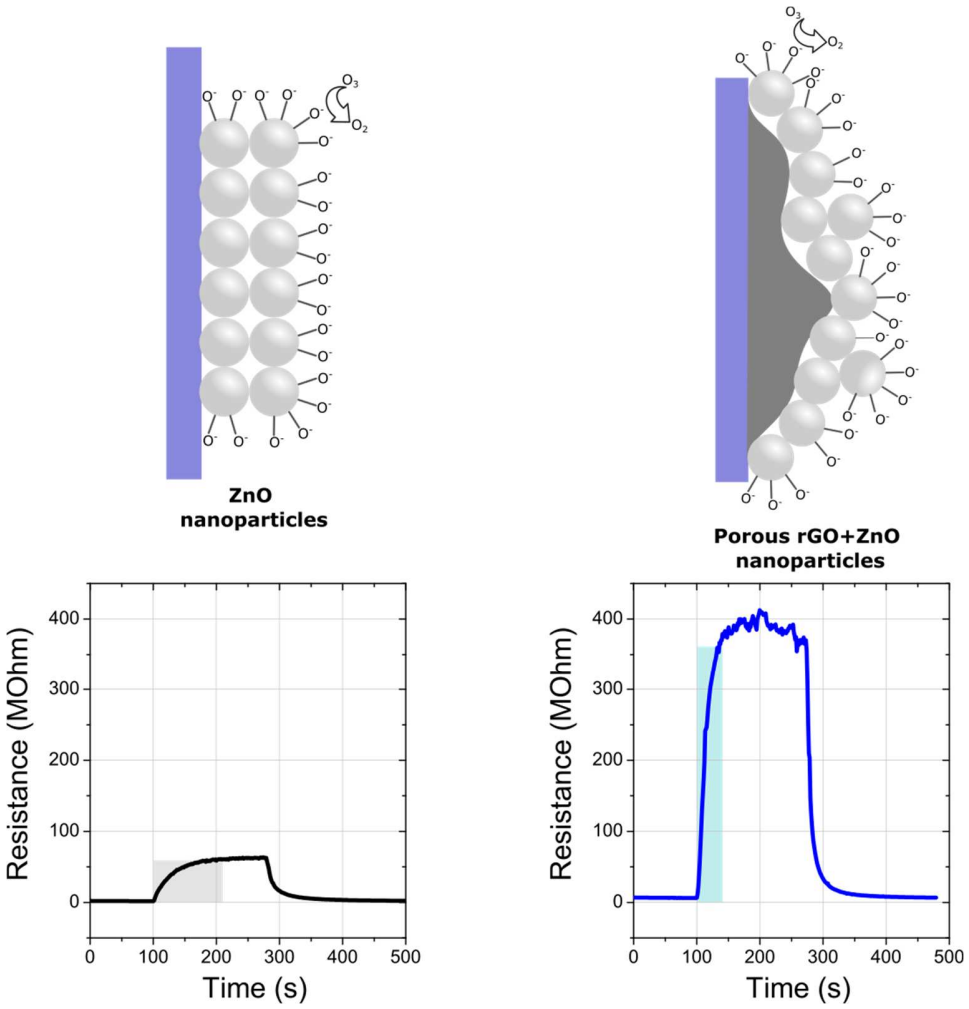

Figure 1. Schematic representation of the experimental setup for the (a) rGO-ZnO nanocomposites preparation and (b) gas sensing properties measurement setup.

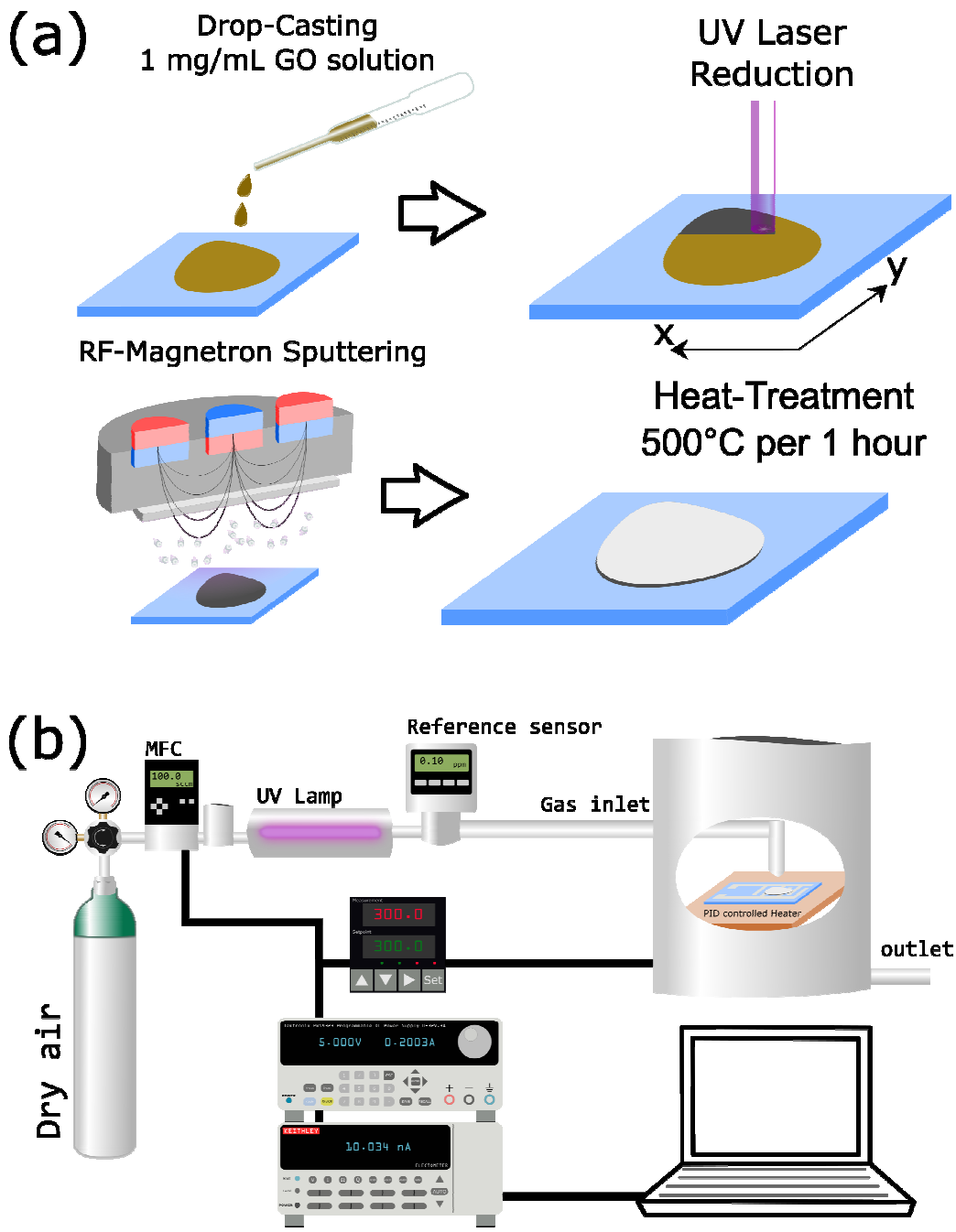

Figure 2. (a) X-ray diffraction and (b) Raman spectroscopy data of GO, rGO, metallic Zn (as deposited by RF-magnetron sputtering), ZnO, and rGO-ZnO nanocomposites.

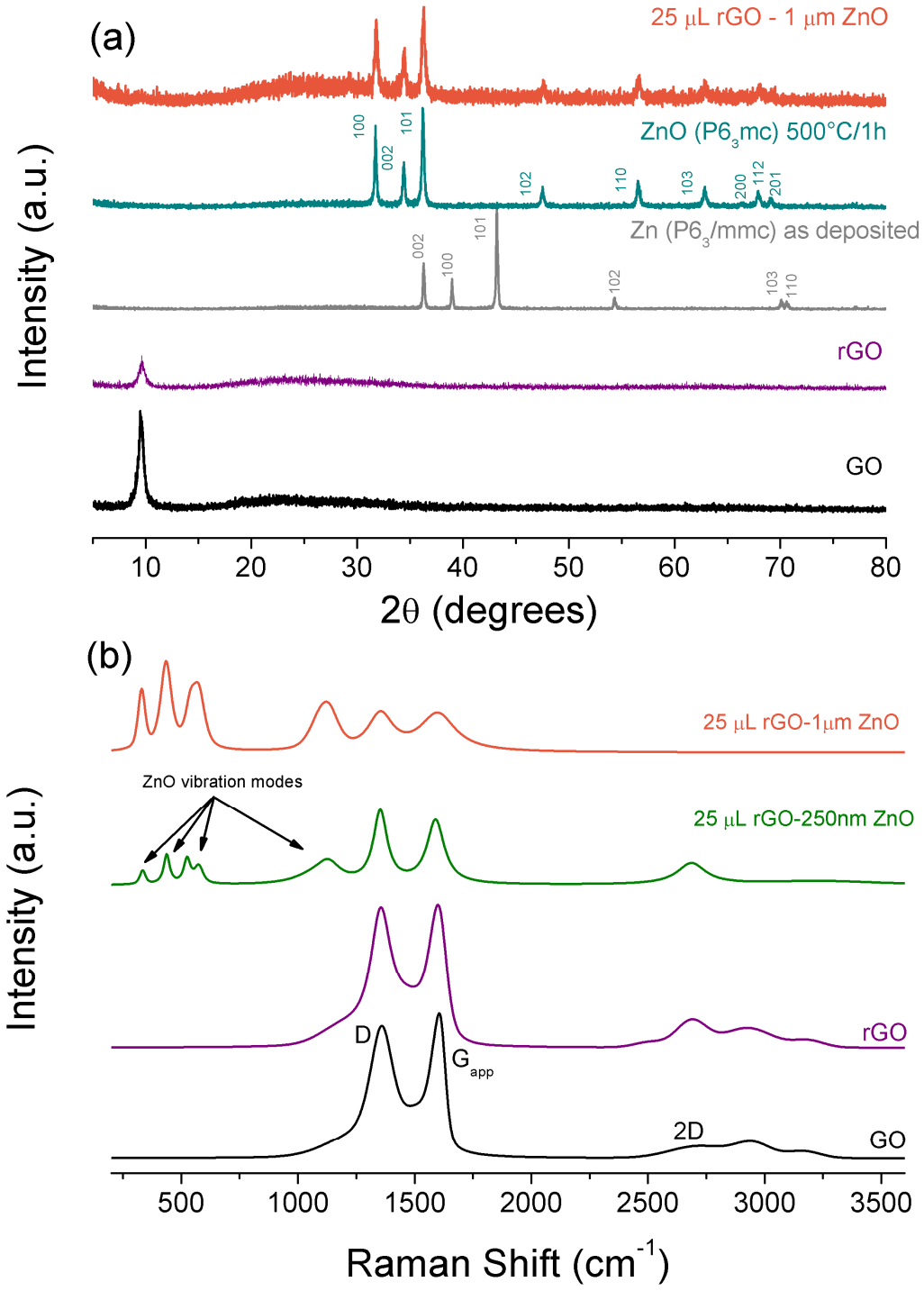

Figure 3. Comparison of XPS (a) survey spectra, (b) C 1s, and (c) O 1s high-resolution regions obtained for GO, laser rGO, pure ZnO, and rGO-ZnO nanocomposites.

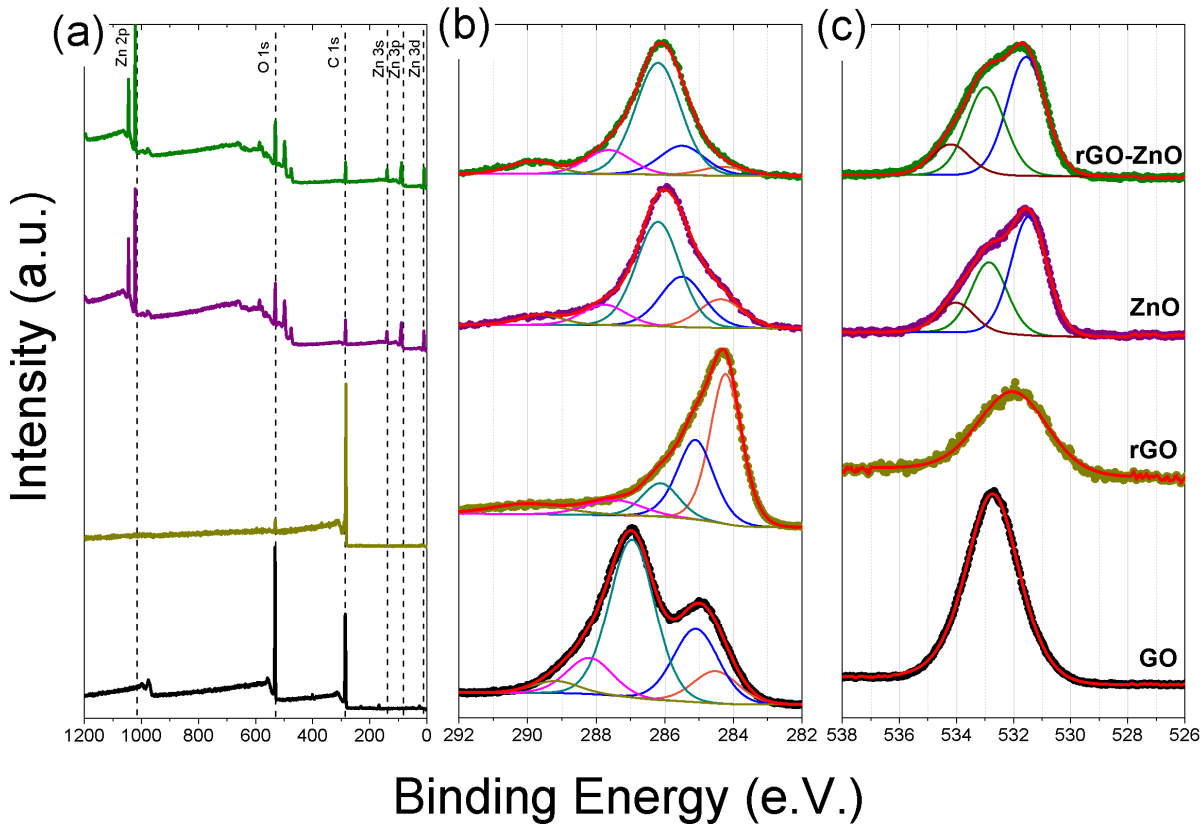

Figure 4. SEM images of GO, rGO and rGO-ZnO nanocomposites. (a) 5k magnification GO, (b) 5x magnification laser rGO, (c) 25k magnification laser rGO, (d) 25k magnification rGO-100nm ZnO, (e) 50k magnification rGO-100nm ZnO, (f) particle size distribution of rGO-100nm ZnO nanocomposites, (g) 25k magnification rGO-1 μm ZnO, (h) 50k magnification rGO-1μm ZnO, and (i) particle size distribution of rGO-1μm ZnO

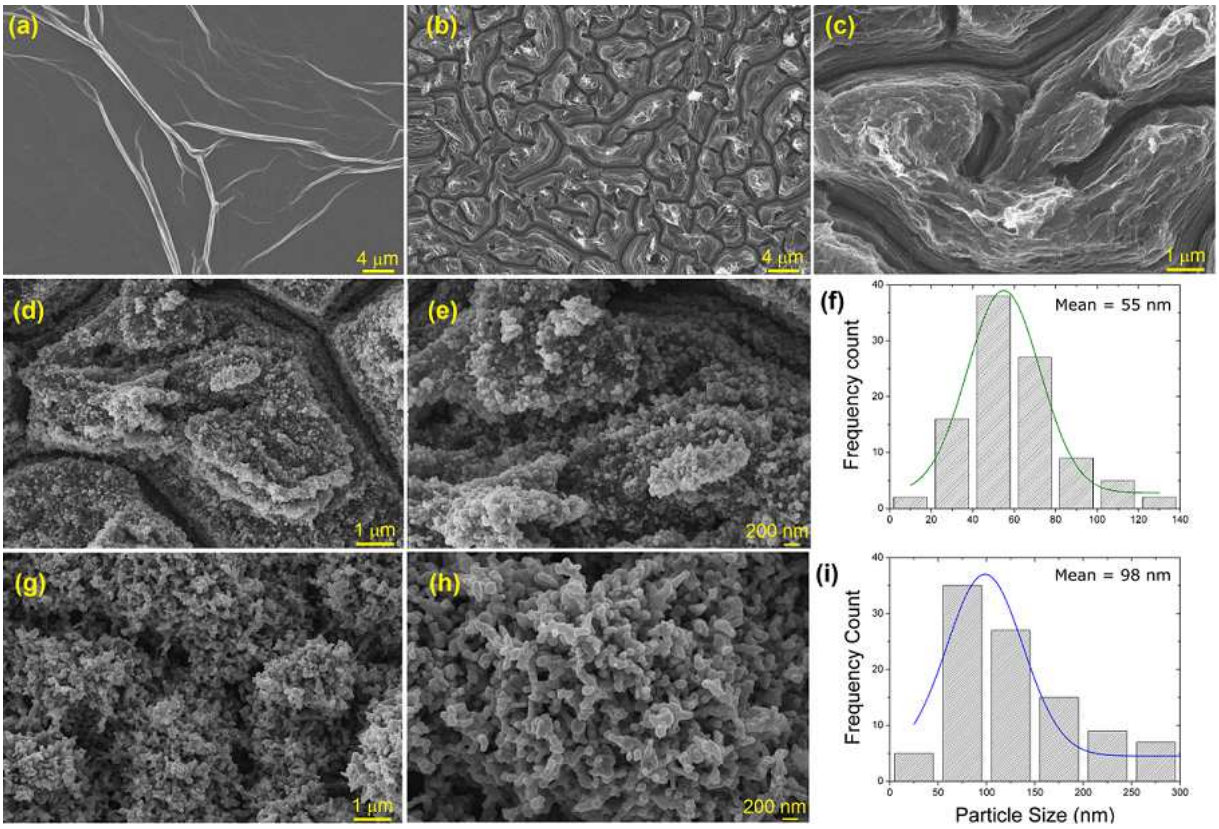

Figure 5. Left panel: Dynamic response-recovery curves at 200°C of (a) pure-rGO, (b) pure ZnO, and (c) rGO-ZnO nanocomposite prepared with three drop-cast cycle deposition of rGO and 100 nm ZnO. Right panel: Dynamic response-recovery curves at 300°C of (d) pure ZnO, (e) rGO-ZnO nanocomposite prepared with one drop-cast cycle deposition of rGO and 100 nm ZnO, and (f) rGO-ZnO nanocomposite prepared with three drop-cast cycle deposition of rGO and 100 nm ZnO.

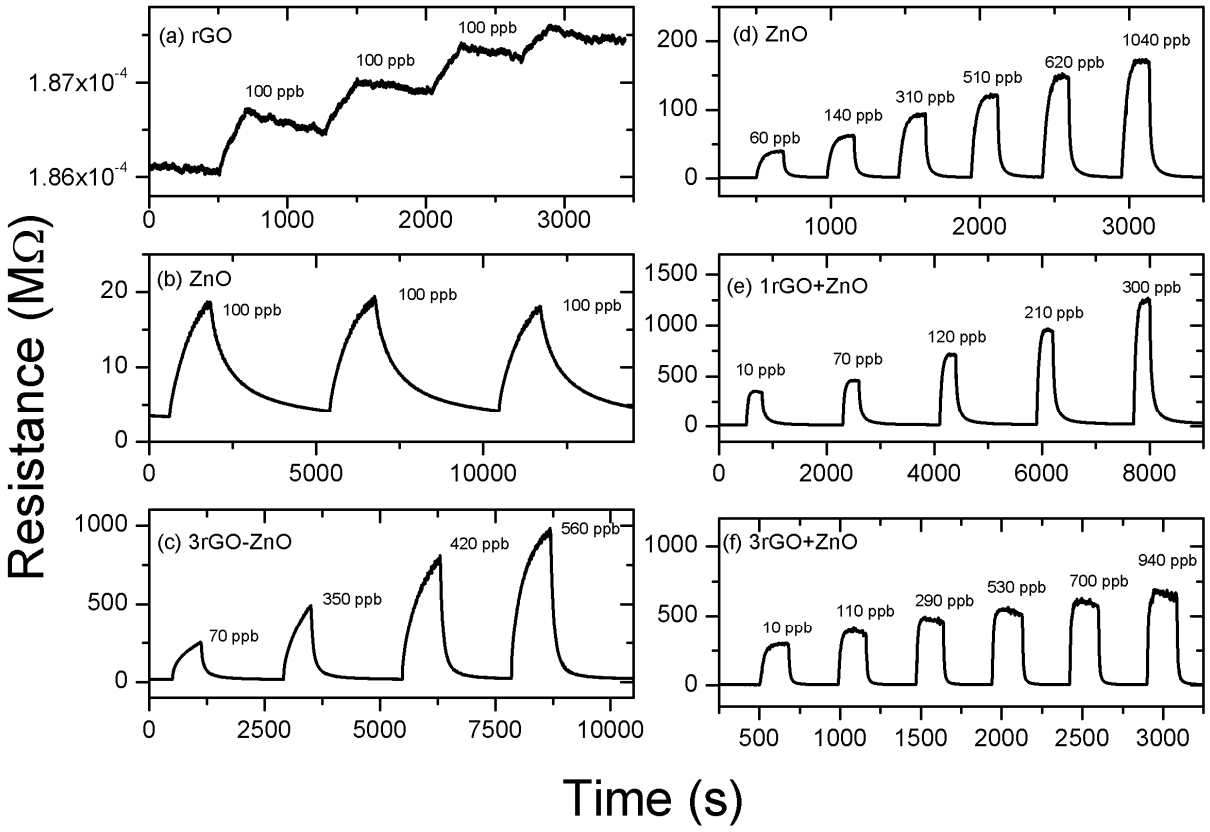

Figure 6. Sensing properties of ZnO (black data) and 3rGO-ZnO (blue data) nanocomposites at 300°C. (a) Dynamic response-recovery curves to 100 ppb of O_3 exposure, (b) Resistance variation (dR/dt) versus time for different O_3 concentration exposures, (c) calibration curves with power-law fitting, (d) response and recovery times. Dashed lines are eye-guides in Figure 6(d).

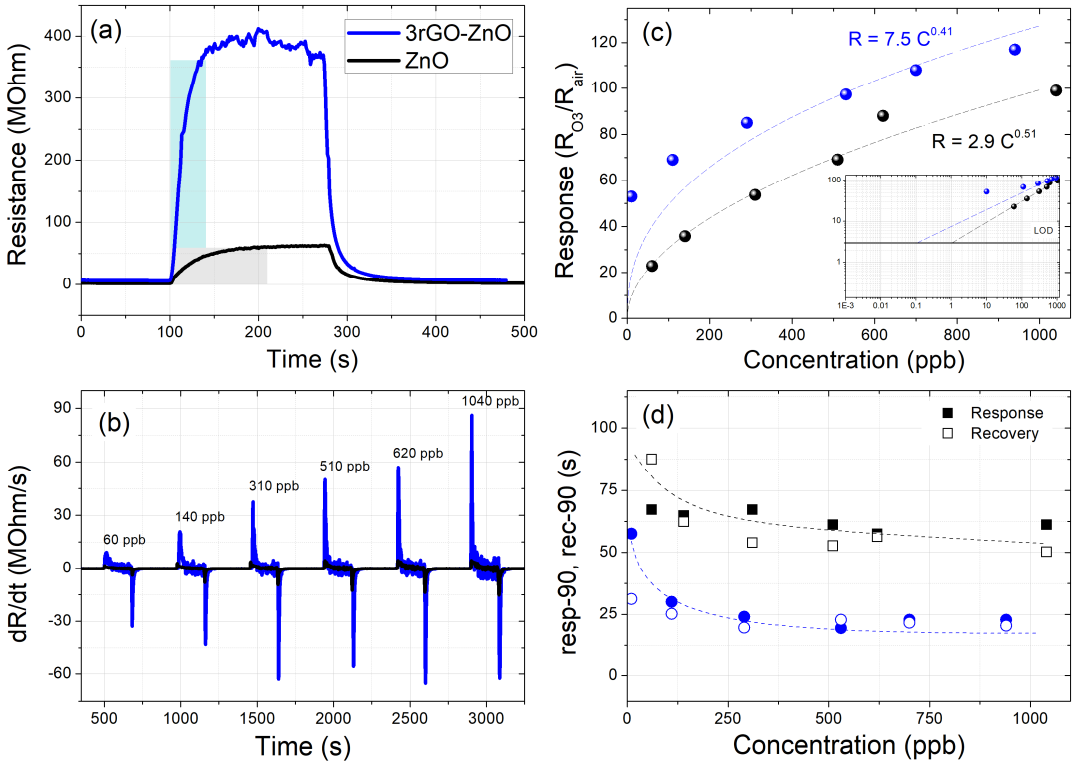

Table 1. Comparison of the ozone performance with the literature

Sensing Material	Operating Temperature (°C)	O_3 concentration (ppb)	O_3 response (R_g/R_{air})	Other Info	Reference
In_2O_3	200	20	6	-	[54]
ZnO	440	1000	1.8	-	[55]
ZnO	300	100	1.91	-	[56]
rGO-ZnO	Room temperature	700	1.97	-	[31]
$CuWO_4$	250	90	10	-	[57]
Co_3O_4	85	100000	130	-	[58]
InGaZnO	Room temperature	1000	13	Under UV light	[59]
Carbon Nanotubes	Room temperature	5000	1.3	-	[60]
rGO-ZnO	300	100	49.6	-	This work

REFERENCES

[1] K.S. Novoselov, A.K. Geim, S.V. Morozov, D. Jiang, Y. Zhang, S.V. Dubonos, I.V. Grigorieva, A.A. Firsov, Electric field effect in atomically thin carbon films, Science, 306 (2004) 666-669.

[2] K.S. Novoselov, A.K. Geim, S.V. Morozov, D. Jiang, M.I. Katsnelson, I.V. Grigorieva, S.V. Dubonos, A.A. Firsov, Two-dimensional gas of massless Dirac fermions in graphene, Nature, 438 (2005) 197-200.

[3] A. Hirsch, The era of carbon allotropes, Nature Materials, 9 (2010) 868-871.

[4] P. Avouris, C. Dimitrakopoulos, Graphene: synthesis and applications, Materials Today, 15 (2012) 86-97.

[5] X. Chen, L. Zhang, S. Chen, Large area CVD growth of graphene, Synthetic Metals, 210 (2015) 95-108.

[6] M. Chen, R.C. Haddon, R. Yan, E. Bekyarova, Advances in transferring chemical vapour deposition graphene: a review, Materials Horizons, 4 (2017) 1054-1063.

[7] D.C. Marcano, D.V. Kosynkin, J.M. Berlin, A. Sinitskii, Z. Sun, A. Slesarev, L.B. Alemany, W. Lu, J.M. Tour, Improved Synthesis of Graphene Oxide, Acs Nano, 4 (2010) 4806-4814.

[8] S.F. Pei, H.M. Cheng, The reduction of graphene oxide, Carbon, 50 (2012) 3210-3228.

[9] J. Yan, J. Liu, Z. Fan, T. Wei, L. Zhang, High-performance supercapacitor electrodes based on highly corrugated graphene sheets, Carbon, 50 (2012) 2179-2188.

[10] D. Bhattacharjya, C.H. Kim, J.H. Kim, I.K. You, J.B. In, S.M. Lee, Fast and controllable reduction of graphene oxide by low-cost CO2 laser for supercapacitor application, Applied Surface Science, 462 (2018) 353-361.

[11] S. Basu, P. Bhattacharyya, Recent developments on graphene and graphene oxide based solid state gas sensors, Sensors and Actuators B-Chemical, 173 (2012) 1-21.

[12] J.T. Robinson, F.K. Perkins, E.S. Snow, Z. Wei, P.E. Sheehan, Reduced Graphene Oxide Molecular Sensors, Nano Letters, 8 (2008) 3137-3140.

[13] B. Cai, S. Wang, L. Huang, Y. Ning, Z. Zhang, G.-J. Zhang, Ultrasensitive Label-Free Detection of PNA-DNA Hybridization by Reduced Graphene Oxide Field-Effect Transistor Biosensor, Acs Nano, 8 (2014) 2632-2638.

[14] K. Krishnamoorthy, R. Mohan, S.J. Kim, Graphene oxide as a photocatalytic material, Applied Physics Letters, 98 (2011).

[15] A.W. Robertson, C.S. Allen, Y.A. Wu, K. He, J. Olivier, J. Neethling, A.I. Kirkland, J.H. Warner, Spatial control of defect creation in graphene at the nanoscale, Nature Communications, 3 (2012).

[16] D. Zhang, H. Chang, P. Li, R. Liu, Q. Xue, Fabrication and characterization of an ultrasensitive humidity sensor based on metal oxide/graphene hybrid nanocomposite, Sensors and Actuators B-Chemical, 225 (2016) 233-240.

[17] H. Zhang, J. Feng, T. Fei, S. Liu, T. Zhang, SnO2 nanoparticles-reduced graphene oxide nanocomposites for NO2 sensing at low operating temperature, Sensors and Actuators B-Chemical, 190 (2014) 472-478.

[18] R.S. Andre, L.A. Mercante, M.H.M. Facure, L.H.C. Mattoso, D.S. Correa, Enhanced and selective ammonia detection using In2O3/reduced graphene oxide hybrid nanofibers, Applied Surface Science, 473 (2019) 133-140.

[19] F. Gu, R. Nie, D. Han, Z. Wang, In2O3-graphene nanocomposite based gas sensor for selective detection of NO2 at room temperature, Sensors and Actuators B-Chemical, 219 (2015) 94-99.

[20] C.W. Na, J.-H. Kim, H.-J. Kim, H.-S. Woo, A. Gupta, H.-K. Kim, J.-H. Lee, Highly selective and sensitive detection of NO2 using rGO-In2O3 structure on flexible substrate at low temperature, Sensors and Actuators B-Chemical, 255 (2018) 1671-1679.

[21] J. Liu, S. Li, B. Zhang, Y. Wang, Y. Gao, X. Liang, Y. Wang, G. Lu, Flower-like In2O3 modified by reduced graphene oxide sheets serving as a highly sensitive gas sensor for trace NO2 detection, Journal of Colloid and Interface Science, 504 (2017) 206-213.

[22] V. Galstyan, E. Comini, I. Kholmanov, G. Faglia, G. Sberveglieri, Reduced graphene oxide/ZnO nanocomposite for application in chemical gas sensors, Rsc Advances, 6 (2016) 34225-34232.

[23] N.B. Thakare, F.C. Raghuwanshi, V.S. Kalyamwar, Y.S. Tamgadge, Reduced Graphene Oxide-ZnO Composites Based Gas Sensors: A Review, in: 2nd International Conference on Condensed Matter and Applied Physics (ICC), Bikaner, INDIA, 2017.

[24] H. Nguyen Hai, T. Dao Duc, H. Nguyen Thanh, P. Nguyen Huy, T. Phan Duy, H. Hoang Si, Fast response of carbon monoxide gas sensors using a highly porous network of ZnO nanoparticles decorated on 3D reduced graphene oxide, Applied Surface Science, 434 (2018) 1048-1054.

[25] A.N.A. Anasthasiya, K.R. Kishore, P.K. Rai, B.G. Jeyaprakash, Highly sensitive graphene oxide functionalized ZnO nanowires for ammonia vapour detection at ambient temperature, Sensors and Actuators B-Chemical, 255 (2018) 1064-1071.

[26] H. Abdollahi, M. Samkan, M.M. Hashemi, Fabrication of rGO nano-sheets wrapped on Ni doped ZnO nanowire p-n heterostructures for hydrogen gas sensing, New Journal of Chemistry, 43 (2019) 19253-19264.

[27] K.S.Y. P. S. Shewale Synthesis and characterization of Cu-doped ZnO/RGO nanocomposites for room-temperature H2S gas sensor, Journal of Alloys and Compounds, 837 (2020) 155527.

[28] R. Peng, Y. Li, J. Chen, P. Si, J. Feng, L. Zhang, L. Ci, Reduced graphene oxide wrapped Au@ZnO core-shell structure for highly selective triethylamine gas sensing application at a low temperature, Sensors and Actuators a-Physical, 283 (2018) 128-133.

[29] Q.A. Drmosh, A.H. Hendi, M.K. Hossain, Z.H. Yamani, R.A. Moqbel, A. Hezam, M. Gondal, UV-activated gold decorated rGO/ZnO heterostructured nanocomposite sensor for efficient room temperature H-2 detection, Sensors and Actuators B-Chemical, 290 (2019) 666-675.

[30] Q.A. Drmosh, Z.H. Yamani, A.H. Hendi, M.A. Gondal, R.A. Moqbel, T.A. Saleh, M.Y. Khan, A novel approach to fabricating a ternary rGO/ZnO/Pt system for high-performance hydrogen sensor at low operating temperatures, Applied Surface Science, 464 (2019) 616-626.

[31] J. Jayachandiran, A. Raja, M. Arivanandhan, R. Jayavel, D. Nedumaran, A facile synthesis of hybrid nanocomposites of reduced graphene oxide/ZnO and its surface modification characteristics for ozone sensing, Journal of Materials Science-Materials in Electronics, 29 (2018) 3074-3086.

[32] J.F.D. Petruci, P.R. Fortes, V. Kokoric, A. Wilk, I.M. Raimundo, A.A. Cardoso, B. Mizaikoff, Real-time monitoring of ozone in air using substrate-integrated hollow waveguide mid-infrared sensors, Scientific Reports, 3 (2013).

[33] R.W. Long, A. Whitehill, A. Habel, S. Urbanski, H. Halliday, M. Colón, S. Kaushik, M.S. Landis, Comparison of Ozone Measurement Methods in Biomass Burning Smoke: An evaluation under field and laboratory conditions, in, 2020.

[34] B.H. Toby, R.B. Von Dreele, GSAS-II: the genesis of a modern open-source all purpose crystallography software package, Journal of Applied Crystallography, 46 (2013) 544-549.

[35] G. Nolze, W. Kraus, PowderCell 2.0 for Windows, Powder Diffraction, 13 (1998) 256-259.

[36] K. Momma, F. Izumi, VESTA 3 for three-dimensional visualization of crystal, volumetric and morphology data, Journal of Applied Crystallography, 44 (2011) 1272-1276.

[37] A.C. Ferrari, J.C. Meyer, V. Scardaci, C. Casiraghi, M. Lazzeri, F. Mauri, S. Piscanec, D. Jiang, K.S. Novoselov, S. Roth, A.K. Geim, Raman spectrum of graphene and graphene layers, Physical Review Letters, 97 (2006).

[38] M.F. Cerqueira, T. Viseu, J.A. de Campos, A.G. Rolo, T. de Lacerda-Aroso, F. Oliveira, I. Bogdanovic-Radovic, E. Alves, M.I. Vasilevskiy, Raman study of insulating and conductive ZnO:(Al, Mn) thin films, Physica Status Solidi a-Applications and Materials Science, 212 (2015) 2345-2354.

[39] R. Al-Gaashani, S. Radiman, A.R. Daud, N. Tabet, Y. Al-Douri, XPS and optical studies of different morphologies of ZnO nanostructures prepared by microwave methods, Ceramics International, 39 (2013) 2283-2292.

[40] J.C. Dupin, D. Gonbeau, P. Vinatier, A. Levasseur, Systematic XPS studies of metal oxides, hydroxides and peroxides, Physical Chemistry Chemical Physics, 2 (2000) 1319-1324.

[41] W.W. Guo, B.Y. Zhao, Q.L. Zhou, Y.Z. He, Z.C. Wang, N. Radacsi, Fe-Doped ZnO/Reduced Graphene Oxide Nanocomposite with Synergic Enhanced Gas Sensing Performance for the Effective Detection of Formaldehyde, Acs Omega, 4 (2019) 10252-10262.

[42] S.A. Ansari, M.H. Cho, Highly Visible Light Responsive, Narrow Band gap TiO2 Nanoparticles Modified by Elemental Red Phosphorus for Photocatalysis and Photoelectrochemical Applications, Scientific Reports, 6 (2016).

[43] B. Gao, T. Wang, X.L. Fan, H. Gong, H. Guo, W. Xia, Y.Y. Feng, X.L. Huang, J.P. He, Synthesis of yellow mesoporous Ni-doped TiO2 with enhanced photoelectrochemical performance under visible light, Inorganic Chemistry Frontiers, 4 (2017) 898-906.

[44] W.K.C. Yung, G.J. Li, H.M. Liem, H.S. Choy, Z.X. Cai, Eye-friendly reduced graphene oxide circuits with nonlinear optical transparency on flexible poly(ethylene terephthalate) substrates, Journal of Materials Chemistry C, 3 (2015) 11294-11299.

[45] T. Nguyen Dien Kha, J. Choi, C.R. Park, H. Kim, Remarkable Conversion Between n- and p-Type Reduced Graphene Oxide on Varying the Thermal Annealing Temperature, Chemistry of Materials, 27 (2015) 7362-7369.

[46] A. Bhaumik, J. Narayan, Conversion of p to n-type reduced graphene oxide by laser annealing at room temperature and pressure, Journal of Applied Physics, 121 (2017).

[47] F. Yang, M.L. Zhao, Z. Wang, H.Y. Ji, B.Z. Zheng, D. Xiao, L. Wu, Y. Guo, The role of ozone in the ozonation process of graphene oxide: oxidation or decomposition?, Rsc Advances, 4 (2014) 58325-58328.

[48] N. Yamazoe, K. Shimanoe, Theory of power laws for semiconductor gas sensors, Sensors and Actuators B-Chemical, 128 (2008) 566-573.

[49] A. Staerz, C. Berthold, T. Russ, S. Wicker, U. Weimar, N. Barsan, The oxidizing effect of humidity on WO3 based sensors, Sensors and Actuators B-Chemical, 237 (2016) 54-58.

[50] S. Wicker, M. Guiltat, U. Weimar, A. Hemeryck, N. Barsan, Ambient Humidity Influence on CO Detection with SnO2 Gas Sensing Materials. A Combined DRIFTS/DFT Investigation, Journal of Physical Chemistry C, 121 (2017) 25064-25073.

[51] G. Korotcenkov, I. Blinov, V. Brinzari, J.R. Stetter, Effect of air humidity on gas response of SnO2 thin film ozone sensors, Sensors and Actuators B-Chemical, 122 (2007) 519-526.

[52] S. Vallejos, I. Gracia, N. Pizurova, E. Figueras, J. Cechal, J. Hubalek, C. Cane, Gas sensitive ZnO structures with reduced humidity-interference, Sensors and Actuators B-Chemical, 301 (2019).

[53] R.L. Fomekong, B. Saruhan, Influence of Humidity on NO2-Sensing and Selectivity of Spray-CVD Grown ZnO Thin Film above 400 degrees C, Chemosensors, 7 (2019).

[54] M.Z. Atashbar, B. Gong, H.T. Sun, W. Wlodarski, R. Lamb, Investigation on ozone-sensitive In2O3 thin films, Thin Solid Films, 354 (1999) 222-226.

[55] F.S.S. Chien, C.R. Wang, Y.L. Chan, H.L. Lin, M.H. Chen, R.J. Wu, Fast-response ozone sensor with ZnO nanorods grown by chemical vapor deposition, Sensors and Actuators B-Chemical, 144 (2010) 120-125.

[56] Y.T. Tsai, S.J. Chang, I.T. Tang, Y.J. Hsiao, L.W. Ji, High Density Novel Porous ZnO Nanosheets Based on a Microheater Chip for Ozone Sensors, Ieee Sensors Journal, 18 (2018) 5559-5565.

[57] A.C. Catto, T. Fiorido, E.L.S. Souza, W. Avansi, J. Andres, K. Aguir, E. Longo, L.S. Cavalcante, L.F. da Silva, Improving the ozone gas-sensing properties of CuWO4 nanoparticles, Journal of Alloys and Compounds, 748 (2018) 411-417.

[58] L.M. Liu, T. Li, Z.C. Yi, F. Chi, Z.D. Lin, X.W. Zhang, K. Xu, Conductometric ozone sensor based on mesoporous ultrafine Co3O4 nanobricks, Sensors and Actuators B-Chemical, 297 (2019).

[59] C.H. Wu, K.W. Chang, Y.N. Li, Z.Y. Deng, K.L. Chen, C.C. Jeng, R.J. Wu, J.H. Chen, Improving the sensitive and selective of trace amount ozone sensor on Indium-Gallium-Zinc Oxide thin film by ultraviolet irradiation, Sensors and Actuators B-Chemical, 273 (2018) 1713-1718.

[60] Q.H. Sun, Z.F. Wu, Y.L. Cao, J.X. Guo, M.Q. Long, H.M. Duan, D.Z. Jia, Chemiresistive sensor arrays based on noncovalently functionalized multi-walled carbon nanotubes for ozone detection, Sensors and Actuators B-Chemical, 297 (2019).